

# Single Electron Precision in the Measurement of Charge Distributions on Electrically Biased Graphene Nanotips Using Electron Holography

Leonardo Vicarelli,<sup>†,||</sup> Vadim Migunov,<sup>\*,‡,§,||</sup> Sairam K. Malladi,<sup>†,⊥</sup> Henny W. Zandbergen,<sup>†</sup> and Rafal E. Dunin-Borkowski<sup>‡</sup>

<sup>†</sup>Kavli Institute of Nanoscience, Delft University of Technology, Lorentzweg 1, 2628 CJ Delft, The Netherlands

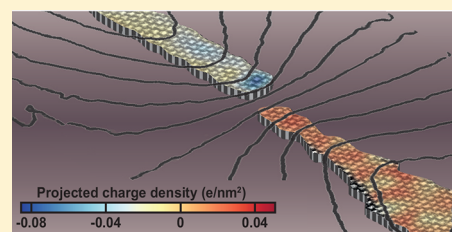
<sup>‡</sup>Ernst Ruska-Centre for Microscopy and Spectroscopy with Electrons and Peter Grünberg Institute, Forschungszentrum Jülich GmbH, 52425 Jülich, Germany

<sup>§</sup>Central Facility for Electron Microscopy, RWTH Aachen University, Ahornstraße 55, 52074 Aachen, Germany

## Supporting Information

**ABSTRACT:** We use off-axis electron holography to measure the electrostatic charge density distributions on graphene-based nanogap devices that have thicknesses of between 1 and 10 monolayers and separations of between 8 and 58 nm with a precision of better than a single unit charge. Our experimental measurements, which are compared with finite element simulations, show that wider graphene tips, which have thicknesses of a single monolayer at their ends, exhibit charge accumulation along their edges. The results are relevant for both fundamental research on graphene electrostatics and applications of graphene nanogaps to single nucleotide detection in DNA sequencing, single molecule electronics, plasmonic antennae, and cold field emission sources.

**KEYWORDS:** Graphene, nanogap, off-axis electron holography, in situ transmission electron microscopy



Graphene nanogap devices that take the form of two graphene electrodes separated by a gap can be used as nanocapacitors, which can be tuned by varying the size of the gap and the dielectric material between the electrodes. The recent fabrication of graphene supercapacitors<sup>1</sup> demonstrates the promise of such devices for both the electronics industry and energy storage applications. Another potential application of graphene nanogaps is in DNA sequencing,<sup>2,3</sup> which involves passing DNA through two electrodes that have a gap of at most 2 nm between them, thereby modulating the tunnelling current. Graphene is currently the best candidate material for this application because of its single-atomic-layer thickness, which allows for single nucleotide detection. In molecular electronics, graphene nanogaps have been used successfully to contact single molecules,<sup>4</sup> replacing traditional Au electrodes. The primary advantages of graphene over Au are its higher melting point (which allows the use of higher currents without electromigration) and the reduced screening of electric fields (which allows external gating to be used). It has also been proposed to replace Au by graphene in dipole antennae for applications as plasmonic (optical) tweezers.<sup>5</sup> Here, the advantages of graphene over Au are its ability to sustain surface plasmons with very low losses in the infrared and terahertz regimes and to enhance electric fields in confined spaces, thereby reducing the laser power needed to trap subwavelength particles. Finally, if a very high electric field is applied across a graphene nanogap in a high vacuum environment, then cold field emission may occur, which is of interest (alongside C nanotubes and nanocones) for future

high brightness and highly stable electron sources for electron microscopes.<sup>6</sup>

In each of these applications, the electric field in the nanogap and the charge density distribution on the graphene electrodes play a fundamental role in the operation of the device. The charge density distributions on large graphene flakes have previously been investigated using scanning tunneling microscopy (STM),<sup>7–9</sup> scanning single electron transistor microscopy (SETSE),<sup>10</sup> and scanning gate microscopy (SGM),<sup>11</sup> in order to visualize the formation of electron-hole puddles near the charge neutrality point (which is achieved at the Dirac point when an equal number of electrons and holes are present in the graphene sheet). STM has also been used to map the electrostatic confinement of Dirac Fermions (electron- and hole-like quasiparticles) in graphene quantum dots.<sup>12</sup> Although STM measurements provide subnanometer spatial resolution and can be used to detect charge density variations as small as  $1 \times 10^9 \text{ e} \cdot \text{cm}^{-2}$ , they require an ultrahigh vacuum environment and cryogenic temperatures and are difficult to scale up to large areas (above  $100 \times 100 \text{ nm}$ ). Whereas SETSE and SGM can be applied at ambient pressure and room temperature and can be used to image larger areas on the order of several  $\mu\text{m}^2$ , their spatial resolution is limited by the size of the tip that is used to

**Received:** April 11, 2019

**Revised:** May 14, 2019

**Published:** May 22, 2019

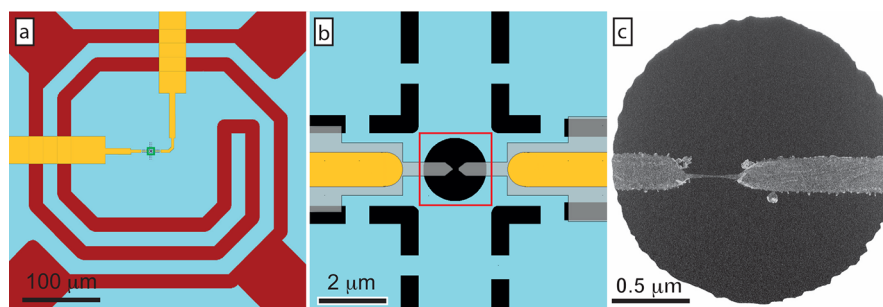


**Figure 1.** (a,b) Schematic diagrams showing a graphene device on a MEMS heating chip. A SiN membrane (blue) supports a heating coil (red), Ti/Pt electrodes (yellow), and the graphene (gray), which spans a hole (black). (c) High-angle annular dark-field STEM image of the area marked with a red square in (b). The light gray contrast corresponds to the central part of the graphene device. This micrograph was recorded before a gap in the bridge was made.

scan the surface, which is typically on the order of tens of nanometers. Furthermore, neither technique can be used to directly measure the electric field distribution of a suspended electrically biased graphene sheet.

Off-axis electron holography is an established technique for the measurement of electrostatic potentials and magnetic fields within and around materials in the transmission electron microscope (TEM). It relies on the use of a coherent electron source to produce a plane electron wave, part of which is allowed to pass through a region of interest in the specimen. This part of the electron wave experiences a phase shift that depends on the local electromagnetic potential. Its interference with a reference part of the same electron wave generates a set of closely spaced interference fringes, in which phase information is recorded. The resulting electron hologram can be reconstructed digitally to retrieve the phase shift of the part of the electron wave that passed through the region of interest. To a first approximation, for a nonmagnetic material the phase shift is directly proportional to the electrostatic potential within and around the sample projected in the electron beam direction, relative to that in the reference region. (Further information about off-axis electron holography, including a ray diagram of the beam path in the TEM, is included in the [Supporting Information](#).)

Off-axis electron holography, in combination with in situ electrical measurements, has previously been used to map local variations in electrostatic potential in samples that include electrically biased W microtips,<sup>13</sup> field emitting C nanotubes,<sup>14</sup> C cone nanotips<sup>15</sup> and p–n junctions in semiconductors.<sup>16</sup> In such applications, careful experimental design can be used to determine and subtract the contribution to the measured phase shift from the mean inner potential (MIP) of the specimen in order to retrieve the electrostatic potential associated with additional charge redistribution, such as that resulting from the presence of an applied voltage. This approach has been used to map charge density distributions in electrically biased Fe atom probe needles,<sup>17</sup> C nanotubes,<sup>18</sup> Ge nanowires undergoing lithiation,<sup>19</sup> and charge-trapping memories.<sup>20</sup>

Here, we use off-axis electron holography together with in situ electrical measurements to study electrostatic charge density distributions in graphene nanogap devices, which consist of two sharp free-standing graphene electrodes that are separated by gaps of between a few nanometers and a few tens of nanometers. Our results provide a precision of better than a single electron in local measurements of charge. We show that the induced charges are localized at the edges of wider graphene tips and compare our measured phase shifts with finite element simulations.

**Experimental Details.** Graphene devices were mounted on custom-designed microelectromechanical systems (MEMS) heating chips, whose fabrication is described elsewhere.<sup>21,22</sup> The device geometry is shown in [Figure 1](#). Each MEMS chip contains a 600  $\mu\text{m}$  wide, 400 nm thick square SiN membrane with an embedded Pt spiral, which can be heated up to 600  $^{\circ}\text{C}$  in a controlled manner. Ti/Pt electrodes were fabricated on the MEMS heating chips using electron beam lithography and lift-off techniques. A 2  $\mu\text{m}$  diameter circular opening was etched in the SiN between the two Ti/Pt electrodes using reactive ion etching. Graphene was exfoliated using the scotch tape method onto a 285 nm thick  $\text{SiO}_2$  substrate, identified using optical microscopy, and transferred onto the SiN opening and the Ti/Pt electrodes using a water-based wedging transfer technique.<sup>23</sup> Adhesion of the graphene to the electrodes was enhanced by baking for 1 h on a hot plate at 120  $^{\circ}\text{C}$ . A 300 nm wide, 2  $\mu\text{m}$  long ribbon was preshaped in the suspended part of the graphene using electron beam lithography and a mild oxygen plasma. The graphene ribbon was then sculpted using the electron beam in an FEI Titan 80-300 TEM, which was operated in scanning TEM (STEM) mode at 300 kV, following steps that are described elsewhere,<sup>24,25</sup> until a narrower (typically 10–30 nm) graphene ribbon was formed.

In situ off-axis electron holography experiments combined with simultaneous electrical biasing were performed in an FEI Titan G2 60-300 TEM operated at 300 kV. This microscope is equipped with a Möllenstedt-type<sup>26</sup> electrostatic biprism located above the first image plane. The biprism potential was set to  $\sim 70$  V, resulting in a holographic interference fringe spacing of 0.43 nm and an overlap width of  $\sim 90$  nm. The typical electron irradiation dose rate during electron hologram acquisition was 5  $\text{e}/\text{s}/\text{\AA}^2$ .

The nanobridges, which typically had lengths of 100–300 nm and widths of 10–100 nm, as well as their contacts, were mechanically very stable. Transfer of the nanobridges from the microscope in which they were sculpted to the microscope in which off-axis electron holography experiments were carried out did not result in any visible changes to their configurations.

Before irradiating each specimen using the electron beam, its temperature was set to 300  $^{\circ}\text{C}$ . At this temperature, electron-beam-induced C deposition is avoided due to the increased surface diffusion of C adatoms and gas molecules and the absence of adsorbed water on the specimen surface.<sup>27,28</sup> Damage to the graphene by electron beam illumination is also reduced due to self-healing effects.<sup>24</sup> In order to form a gap in each ribbon, the voltage was ramped up to  $\sim 3$  V at a constant rate of 0.08 V/s. Gap formation was typically observed at a current

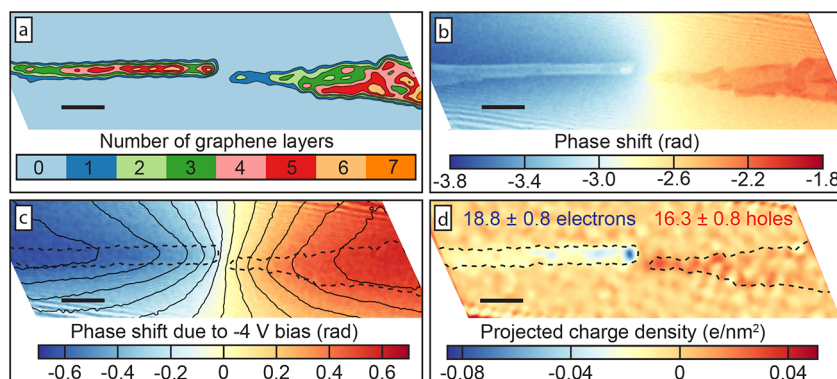


**Figure 2.** Charge measurement in closely spaced graphene nanotips. (a) Electron phase shift at 0 V bias shown in units of the number of graphene layers (assuming a phase shift of 30 mrad per graphene layer at 300 kV<sup>31,32</sup>). (b) Electron phase shift measured at  $-4$  V bias showing the sum of the mean inner potential contribution to the phase shift of the graphene tips measured in (a) and an additional contribution from the projected electrostatic potential associated with the presence of induced charge on each tip. (c) Difference between phase images recorded at 0 and  $-4$  V bias. The black solid lines and dashed lines show equiphase contours separated by 0.1 radians and the outlines of the tip edges, respectively. (d) Laplacian of the phase difference image in (c), showing the projected charge density inside each graphene nanotip. The dashed lines show the outlines of the tip edges, within which the projected charge density was integrated, resulting in measured values of  $18.8 \pm 0.8$  electrons in the left tip and  $16.3 \pm 0.8$  holes in the right tip. Scale bar: 20 nm.

density of  $\sim 5 \times 10^8$  A·cm<sup>-2</sup>, which induced breakdown due to electromigration, similar to the procedure described by Nguyen et al.<sup>29</sup> (see the Supporting Information for further details and Figure S3 for a current–voltage ( $I$ – $V$ ) plot). After the formation of a nanogap, the temperature was reduced to ambient temperature and off-axis electron holograms were recorded with bias voltages of 0, +4, and  $-4$  V applied across it. In order to correct for phase distortions of the imaging and recording system of the TEM, a reference electron hologram was recorded from a field-free vacuum region at zero bias voltage after shifting the specimen by  $\sim 15$   $\mu$ m. Electron holograms were reconstructed using a standard Fourier space method involving recentering and filtering a sideband, followed by inverse fast Fourier transformation.<sup>30</sup> All image processing, including image alignment and numerical calculations of phase differences and Laplacians (see below), was carried out using scripts written in the MathWorks Matlab software package.

**Results and Discussion.** A prepatterned graphene ribbon was decomposed into two closely spaced nanotips in situ in the TEM by passing a current through it. The electron phase shift, which is proportional to the projected electrostatic potential for a weakly diffracting nonmagnetic sample, was measured using off-axis electron holography and is shown in Figure 2. First, the number of graphene layers in each tip was measured at zero bias voltage in units of the mean phase shift produced by a single graphene monolayer, which is  $\sim 50$  mrad at 80 kV and  $\sim 30$  mrad at 300 kV (used here),<sup>31,32</sup> as shown in Figure 2a. For graphene examined in plan-view geometry, the relationship between phase shift and specimen thickness is approximately linear up to a thickness of several tens of nanometers.<sup>31,33</sup> No significant structural damage was observed during sculpting of the graphene bridges, which is in agreement with previous work on graphene sculpting using the same parameters.<sup>25</sup>

In the nanobridge shown in Figure 2, the tips have thicknesses of 1–5 monolayers in most regions. The left tip is relatively homogeneous with a thicker (six monolayer) region at its apex. The right tip has a single monolayer region at its apex and a tapered shank. The application of a bias voltage between the tips results in a three-dimensional variation in electrostatic potential between them. The MIP contribution to the phase recorded at 0 V bias was subtracted from the total phase shift recorded at a bias

voltage of  $-4$  V (Figure 2b) to obtain a phase image associated with charge redistribution alone (Figure 2c). It should be noted that both phase images (before and after subtracting the MIP contribution) suffer from the presence of a perturbed reference wave (PRW), which is associated with the long-range electrostatic field originating from the specimen.<sup>34</sup> This effect can be seen in Figure 2c in the form of asymmetry of the phase contours with respect to the tip axis.

The projected charge density distribution induced in the tips by the application of a bias voltage can be deduced from the Laplacian of the phase difference image in Figure 2c, as shown in Figure 2d. In such a measurement, artifacts associated with the PRW are avoided, as the reference wave does not contain any charges.<sup>17</sup> The projected charge density distribution in Figure 2d is concentrated at the apex of each tip. In addition, there is an accumulation of charge in a thicker (dot-shaped) region in the left tip (dark blue spot in Figure 2d). By integrating the projected charge density in the areas marked with dashed lines in Figure 2d, we find that the left tip has  $18.8 \pm 0.8$  electrons, whereas the right tip has  $16.3 \pm 0.8$  holes. (An explanation of the errors in the measured values is given in the Supporting Information.) Although the integration areas are different (612 nm<sup>2</sup> for the left tip and 1000 nm<sup>2</sup> for the right tip), the asymmetry in the accumulated charge is in the opposite sense. The origin of the 20% difference in total charge between the tips is discussed below.

Our measurements of accumulated charge can be used to determine a value for the capacitance of the nanotips (determined by dividing the measured charge by the applied voltage) of 0.7 aF. The capacitance of the entire device, including the charge in the graphene regions that are outside the field of view, is addressed using simulations below. The use of cumulative acquisition techniques in off-axis electron holography,<sup>35</sup> combined with the present method for extracting the total charge from the Laplacian of the phase difference image,<sup>17,36</sup> allows the charge of a single electron to be resolved in real space. The error can be estimated from the variation in the total charge measured using different integration areas (as described in the Supporting Information, see Figure S6). In our experiments, a potential of 15 V could be applied safely to the device for a separation between the tips of a few tens of

nanometers. A charge of one electron at an applied voltage of 15 V would correspond to a detectable capacitance for a similar nanotip geometry of 10 zF. Such a sensitivity, combined with subnanometer spatial resolution, makes off-axis electron holography a powerful technique for charge and capacitance measurement at the nanoscale.

We repeated the measurements for three different devices in total (as summarized in the Supporting Information) with gaps between the tips of between 8 and 58 nm. The measured capacitance values varied between 0.7 and 4 aF. Interestingly, different devices showed different charge accumulation behavior. For wider and thicker tips, the charge was located at their apexes and edges, whereas for thinner and smaller devices the charge was located primarily at their apexes with a fraction of it located in their volumes (compare Figures 2d and S4d).

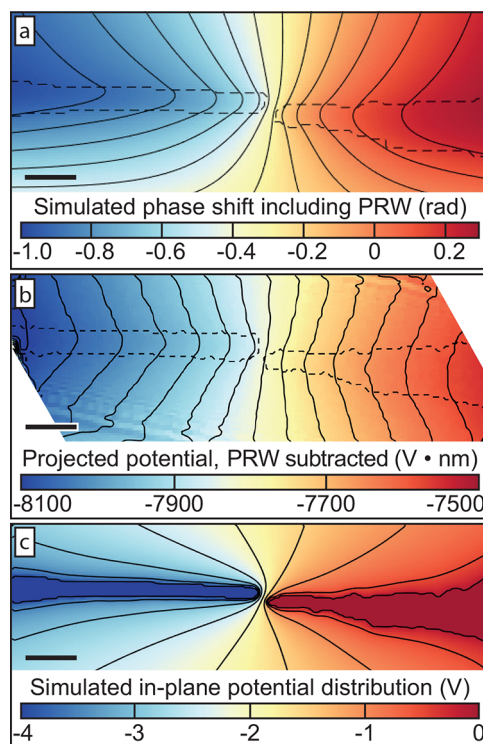
In order to assess differences between the devices, as well as the unbalanced charge described above and nonclassical effects such as quantum capacitance, we performed finite element method (FEM) simulations. The geometries of the devices were reproduced with the help of low-magnification STEM images. Each model included the SiN supporting membrane and the graphene tips up to the contact with the metal, resulting in simulated areas that were more than 20 times the electron holographic field of view. The graphene tips themselves were modeled as two-dimensional charged planes. (Further details are available in the Supporting Information.)

Figure 3a shows the simulated electron phase shift for the graphene nanogap device shown in our experimental measurement for an applied potential difference of 4 V. The perturbed reference wave was included in the simulations by subtracting the phase shift from a neighboring region, which was identified using the experimentally measured biprism angle and interference distance. The total phase shift is given by the expression

$$\phi_T(\mathbf{r}) = \phi(\mathbf{r}) - \phi(\mathbf{r} + \mathbf{D}) \quad (1)$$

where  $\mathbf{D}$  is the interference vector and  $\mathbf{r}$  is an in-plane position vector. Further details can be found in the Supporting Information. A schematic diagram of the experimental geometry for off-axis electron holography, which explains the PRW effect, is shown in Figure S10.

The simulation in Figure 3a shows a remarkably close match to the experimental phase image shown in Figure 2c. The projected potential only faintly resembles the geometry of the tips due to the presence of strong electrostatic fringing fields originating from both the tips and the larger parts of the graphene device that are outside the field of view (see Figure 1). In contrast, an in-plane slice through the simulated electrostatic potential shows that the true three-dimensional equipotential surfaces coincide with the edges of the tips (Figure 3c). The good agreement between the experimental results and the simulations, in terms of both the amount of charge and the shape of the phase shift, suggests that even thin (1–2 monolayer) graphene behaves electrostatically similarly to a metal for the charge densities studied here. The measured charge asymmetry, which was reproduced in the simulation with 16.2 electrons in the left tip and 13.1 holes in the right tip, is attributed to the asymmetric geometry of the device, which is visible in Figure 1c. In response to the applied bias voltage, the left tip (which has a smaller area) acquires a larger charge density than the right tip (which has a larger area). The capacitance of the entire device (including the regions outside the field of view) was determined from the simulations to be  $\sim 12.5$  aF.



**Figure 3.** Simulations of the electrostatic phase shift of a graphene nanogap device. (a) Simulated phase shift including the effect of the perturbed reference wave (PRW). The equiphase contours (solid black lines) have a separation of 0.1 radians. Here and in (b), the edges of the graphene tips are outlined with dashed black lines. (b) True experimental projected electrostatic potential obtained by subtracting the projected potential of the simulated perturbed reference wave from the original experimentally measured projected electrostatic potential. The contour separation is 40 V·nm. (c) Slice through the simulated three-dimensional electrostatic potential in the plane of the graphene device. The contour separation is 0.5 V. The  $-4$  and  $0$  V contours coincide with the graphene nanotip edges. Scale bar: 20 nm.

The total charge measured experimentally is higher than the simulated charge by  $\sim 20\%$ , most likely due to the slight differences between the modeled and experimental geometries, including the definition of the graphene edges and the finite thicknesses of the graphene tips. In order to address other possible origins of this discrepancy, we briefly consider the influence of quantum capacitance,<sup>37</sup> edge states, leakage currents, changes in tip separation due to Coulomb forces, and electron-beam-induced effects. Quantum capacitance, which arises due to the small density of states in graphene at the Dirac point, is expected to reduce the experimentally measured charge, compared to simulations in which quantum effects are not considered. Recent experimental studies<sup>38,39</sup> have reported negative quantum capacitance in graphene, either due to strong electron–electron interactions in back-gated devices or due to reduced screening by graphene side gates. Detailed quantum mechanical simulations, which are beyond the scope of the present work, are required to address the influence of quantum capacitance on such measurements in detail. Although a leakage current can arise due to parasitic conductance of the supporting SiN membrane or a tunnelling current between the tips, such a leakage current would not have affected the charge that we measured in our device and was below 7 nA (the noise level in our electrical setup) at room temperature and 4 V bias. (We observed field emission at higher applied voltages, as

discussed below; further details, including  $I$ – $V$  plots, can be found in the [Supporting Information](#).) With regard to the effect of an attractive Coulomb force, we did not observe any change in distance between the tips to within our spatial resolution, which is approximately 1.3 nm. Our simulations suggest that such a difference would result in a change of only 0.15 units of charge (approximately 1% of the total measured charge). We can also exclude electron beam effects, as they act on the negatively and positively charged tips with the same sign. In order to assess the possibility of small geometrical discrepancies between the model used in the simulations and the real device, we repeated our simulations by varying three geometrical parameters: the separation of the tips, their width, and their thickness. We were able to match the experimental values of total charge on both tips by reducing the gap size in the simulations by  $\sim 30\%$  or by increasing the tip width by  $\sim 16\%$ . The experimental values could also be reached for nanotips that are thicker than four monolayers (see [Table S2](#) in the [Supporting Information](#)). Electrostatic simulations of graphene nanotips that take regions of different thickness into account would require more sophisticated modeling.

By comparing measurements performed on different devices with each other (see the [Supporting Information](#)), we found better agreement between simulated and experimental charge densities for thicker devices (containing more than four graphene layers). These devices also have larger gaps (of up to 58 nm), meaning that small discrepancies between the real and simulated geometries do not play a significant role as in the device presented above. The thicker and larger devices also show clearer accumulation of charge at their edges. This behavior may be associated with the fact that multilayer graphene is metallic, whereas a single layer can be semiconducting with a zero bandgap, or alternatively due to the lateral resolution of the analysis of 3 nm, which is only barely sufficient to resolve charged edge layers in an 8 nm wide ribbon. The latter source of error could be improved by using a lower electron beam energy (to increase the interaction constant and therefore increase the phase shift, while decreasing damage to the graphene) or by increasing the spatial resolution or acquisition time.

In addition to electrostatic measurements, we attempted to induce field emission from one tip to the other. Although we were technically limited in the voltage that we could apply, we were able to observe field emission for one of the devices (device 1 in the [Supporting Information](#)). The field emission current was stable between 15 and 22 V, reaching a maximum of 0.5  $\mu\text{A}$ . From a Fowler–Nordheim plot<sup>40</sup> (see [Figure S11](#) in the [Supporting Information](#)), we determined a field enhancement factor  $\beta$  of  $22 \pm 7$ , assuming a constant graphene work function  $\phi$  of  $\sim 5$  eV. Comparable values have been obtained for field-emitting C cone nanotips<sup>41</sup> and C nanotubes with similar length-to-width ratios.<sup>42</sup> Higher field enhancement factors could be achieved in future experiments by fabricating longer and narrower graphene tips.

In conclusion, the projected charge density in closely spaced graphene nanotips has been measured using off-axis electron holography with a precision of better than a single electron. The charge density within the field of view corresponds to a measured capacitance of 0.7 aF. Finite element simulations of the three-dimensional electrostatic potential around the device show an almost perfect match with the experimentally measured projected potential. Small discrepancies between the experimental and simulated charge densities may result from geometrical inaccuracies in the model used in the simulations

or effects that are difficult to assess at present, such as edge states or quantum capacitance. Our results suggest that the graphene in such a nanogap device can be treated as a single conducting layer with no additional screening of the electric field, which is in contrast to previous observations in the literature.<sup>43,44</sup> Improvements in the sensitivity and spatial resolution of charge detection could be achieved in future experiments by using cumulative acquisition of electron holograms and aberration corrected imaging. Temperature-dependent studies could also be used to assess quantum effects experimentally. In addition to fundamental interest in charge redistribution in monolayer and few-layer graphene, our results are of interest for the design and fabrication of nanogap devices for single molecule electronics, DNA sequencing, plasmonic optical tweezers, and cold field emission sources.

## ■ ASSOCIATED CONTENT

### Supporting Information

The Supporting Information is available free of charge on the [ACS Publications website](#) at DOI: [10.1021/acs.nanolett.9b01487](https://doi.org/10.1021/acs.nanolett.9b01487).

Further technical information and information regarding other devices ([PDF](#))

## ■ AUTHOR INFORMATION

### Corresponding Author

\*E-mail: [v.migunov@fz-juelich.de](mailto:v.migunov@fz-juelich.de).

### ORCID

Vadim Migunov: [0000-0002-6296-4492](https://orcid.org/0000-0002-6296-4492)

### Present Addresses

<sup>||</sup>(L.V.) Dipartimento di Fisica “E. Fermi”, Università di Pisa and NEST, CNR-Istituto Nanoscienze e Scuola Normale Superiore, Piazza San Silvestro 12, 56127 Pisa, Italy.

<sup>⊥</sup>(S.K.M.) Department of Materials Science and Metallurgical Engineering, Indian Institute of Technology Hyderabad, Yeddumailaram 502205, Andhra Pradesh, India.

### Notes

The authors declare no competing financial interest.

## ■ ACKNOWLEDGMENTS

The authors are grateful to Beata Kardynał, Florian Winkler, Giulio Pozzi, and Fengshan Zheng for valuable discussions and assistance. We also thank Werner Pieper for technical aid. L.V. and H.W.Z. acknowledge the European Research Council (ERC) project number 267922 for funding. V.M. acknowledges the Deutsche Forschungsgemeinschaft for funding within the framework of the SFB917 collaborative research center. This project has received funding from the European Union's Horizon 2020 research and innovation programme under Grant Agreement 823717-ESTEEM3.

## ■ REFERENCES

- (1) Stoller, M. D.; Park, S.; Yanwu, Z.; An, J.; Ruoff, R. S. Graphene-Based ultracapacitors. *Nano Lett.* **2008**, *8*, 3498–3502.
- (2) Postma, H. W. Ch. Rapid sequencing of individual DNA molecules in graphene nanogaps. *Nano Lett.* **2010**, *10*, 420–425.
- (3) Heerema, S. J.; Dekker, C. Graphene nanodevices for {DNA} sequencing. *Nat. Nanotechnol.* **2016**, *11*, 127–136.
- (4) Prins, F.; Barreiro, A.; Ruitenbergh, J. W.; Seldenthuis, J. S.; Aliaga-Alcalde, N.; Vandersypen, L. M. K.; van der Zant, H. S. J. Room-temperature gating of molecular junctions using few-layer graphene nanogap electrodes. *Nano Lett.* **2011**, *11*, 4607–4611.

- (5) Kim, J.-D.; Lee, Y.-G. Graphene based plasmonic tweezers. *Carbon* **2016**, *103*, 281–290.
- (6) Houdellier, F.; de Knoop, L.; Gatel, C.; Masseboeuf, A.; Mamishin, S.; Taniguchi, Y.; Delmas, M.; Monthieux, M.; Hÿtch, M. J.; Snoeck, E. Development of TEM and SEM high brightness electron guns using cold-field emission from a carbon nanotip. *Ultramicroscopy* **2015**, *151*, 107–115.
- (7) Zhang, Y.; Brar, V. W.; Girit, C.; Zettl, A.; Crommie, M. F. Origin of spatial charge inhomogeneity in graphene. *Nat. Phys.* **2009**, *5*, 722–726.
- (8) Samaddar, S.; Yudhistira, I.; Adam, S.; Courtois, H.; Winkelmann, C. B. Charge Puddles in Graphene near the Dirac Point. *Phys. Rev. Lett.* **2016**, *116*, 126804.
- (9) Decker, R.; Wang, Y.; Brar, V. W.; Regan, W.; Tsai, H.-Z.; Wu, Q.; Gannett, W.; Zettl, A.; Crommie, M. F. Local Electronic Properties of Graphene on a BN Substrate via Scanning Tunneling Microscopy. *Nano Lett.* **2011**, *11*, 2291–2295.
- (10) Martin, J.; Akerman, N.; Ulbricht, G.; Lohmann, T.; Smet, J. H.; von Klitzing, K.; Yacoby, A. Observation of Electron-Hole Puddles in Graphene Using a Scanning Single Electron Transistor. *Nat. Phys.* **2008**, *4*, 144–148.
- (11) Jalilian, R.; Jauregui, L. A.; Lopez, G.; Tian, J.; Roecker, C.; Yazdanpanah, M. M.; Cohn, R. W.; Jovanovic, I.; Chen, Y. P. Scanning gate microscopy on graphene: charge inhomogeneity and extrinsic doping. *Nanotechnology* **2011**, *22*, 295705.
- (12) Lee, J.; Wong, D.; Velasco, J.; Rodriguez-Nieva, J. F.; Kahn, S.; Tsai, H.-Z.; Taniguchi, T.; Watanabe, K.; Zettl, A.; Wang, F.; Levitov, L. S.; Crommie, M. F. Imaging electrostatically confined Dirac fermions in graphene quantum dots. *Nat. Phys.* **2016**, *12*, 1032.
- (13) Matteucci, G.; Missiroli, G. F.; Muccini, M.; Pozzi, G. Electron holography in the study of the electrostatic fields: the case of charged microtips. *Ultramicroscopy* **1992**, *45*, 77–83.
- (14) Cumings, J.; Zettl, A.; McCartney, M. R.; Spence, J. C. H. Electron Holography of Field-Emitting Carbon Nanotubes. *Phys. Rev. Lett.* **2002**, *88*, 056804.
- (15) de Knoop, L.; Gatel, C.; Houdellier, F.; Monthieux, M.; Masseboeuf, A.; Snoeck, E.; Hÿtch, M. J. Low-noise cold-field emission current obtained between two opposed carbon cone nanotips during in situ transmission electron microscope biasing. *Appl. Phys. Lett.* **2015**, *106*, 263101.
- (16) Twitchett, A. C.; Dunin-Borkowski, R. E.; Hallifax, R. J.; Broom, R. F.; Midgley, P. A. Off-axis electron holography of electrostatic potentials in unbiased and reverse biased focused ion beam milled semiconductor devices. *J. Microsc.* **2004**, *214*, 287–296.
- (17) Migunov, V.; London, A.; Farle, M.; Dunin-Borkowski, R. E. Model-independent measurement of the charge density distribution along an Fe atom probe needle using off-axis electron holography without mean inner potential effects. *J. Appl. Phys.* **2015**, *117*, 134301.
- (18) Beleggia, M.; Kasama, T.; Dunin-Borkowski, R. E.; Hofmann, S.; Pozzi, G. Direct measurement of the charge distribution along a biased carbon nanotube bundle using electron holography. *Appl. Phys. Lett.* **2011**, *98*, 243101.
- (19) Gan, Z.; Gu, M.; Tang, J.; Wang, C.-Y.; He, Y.; Wang, K. L.; Wang, C.; Smith, D. J.; McCartney, M. R. Direct Mapping of Charge Distribution during Lithiation of Ge Nanowires Using Off-Axis Electron Holography. *Nano Lett.* **2016**, *16*, 3748–3753.
- (20) Yao, Y.; Li, C.; Huo, Z. L.; Liu, M.; Zhu, C. X.; Gu, C. Z.; Duan, X. F.; Wang, Y. G.; Gu, L.; Yu, R. C. In situ electron holography study of charge distribution in high- $\kappa$  charge-trapping memory. *Nat. Commun.* **2013**, *4*, 2764.
- (21) Creemer, J.; Briand, D.; Zandbergen, H.; van der Vlist, W.; de Boer, C.; de Rooij, N.; Sarro, P. Microhotplates with TiN heaters. *Sens. Actuators, A* **2008**, *148*, 416–421.
- (22) Creemer, J.; Helveg, S.; Hoveling, G.; Ullmann, S.; Molenbroek, A.; Sarro, P.; Zandbergen, H. Atomic-scale electron microscopy at ambient pressure. *Ultramicroscopy* **2008**, *108*, 993–998.
- (23) Schneider, G. F.; Calado, V. E.; Zandbergen, H.; Vandersypen, L. M. K.; Dekker, C. Wedging transfer of nanostructures. *Nano Lett.* **2010**, *10*, 1912–1916.
- (24) Song, B.; Schneider, G. F.; Xu, Q.; Pandraud, G.; Dekker, C.; Zandbergen, H. Atomic-scale electron-beam sculpting of near-defect-free graphene nanostructures. *Nano Lett.* **2011**, *11*, 2247–2250.
- (25) Xu, Q.; Wu, M.-Y.; Schneider, G. F.; Houben, L.; Malladi, S. K.; Dekker, C.; Yucelen, E.; Dunin-Borkowski, R. E.; Zandbergen, H. W. Controllable Atomic Scale Patterning of Freestanding Monolayer Graphene at Elevated Temperature. *ACS Nano* **2013**, *7*, 1566–1572.
- (26) Möllenstedt, G.; Düker, H. Beobachtungen und Messungen an Biprisma-Interferenzen mit Elektronenwellen. *Eur. Phys. J. A* **1956**, *145*, 377–397.
- (27) Wei, X. L.; Liu, Y.; Chen, Q.; Peng, L. M. Controlling electron-beam-induced carbon deposition on carbon nanotubes by Joule heating. *Nanotechnology* **2008**, *19*, 355304.
- (28) Hart, R. K.; Kassner, T. F.; Maurin, J. K. The contamination of surfaces during high-energy electron irradiation. *Philos. Mag.* **1970**, *21*, 453–467.
- (29) Nguyen, P. D.; Nguyen, T. C.; Hossain, F. M.; Huynh, D. H.; Evans, R.; Skafidas, E. Negative differential resistance effect in planar graphene nanoribbon break junctions. *Nanoscale* **2015**, *7*, 289–293.
- (30) Tonomura, A. *Electron Holography*, 2nd ed.; Springer Series in Optical Sciences; Springer, 1999.
- (31) Ortolani, L.; Houdellier, F.; Monthieux, M.; Snoeck, E.; Morandi, V. Surface electrostatic potentials in carbon nanotubes and graphene membranes investigated with electron holography. *Carbon* **2011**, *49*, 1423–1429.
- (32) Cooper, D.; Pan, C.-T.; Haigh, S. Atomic resolution electrostatic potential mapping of graphene sheets by off-axis electron holography. *J. Appl. Phys.* **2014**, *115*, 233709.
- (33) Dunin-Borkowski, R. E.; Boothroyd, C. B.; Beleggia, M. Dynamical Effects in the Study of Supported Nanocrystals using Electron Holography. *Microsc. Microanal.* **2010**, *16*, 572–573.
- (34) Matteucci, G.; Missiroli, G.; Nichelatti, E.; Migliori, A.; Vanzi, M.; Pozzi, G. Electron holography of long-range electric and magnetic fields. *J. Appl. Phys.* **1991**, *69*, 1835–1842.
- (35) Voelkl, E.; Tang, D. Approaching routine  $2\pi/1000$  phase resolution for off-axis type holography. *Ultramicroscopy* **2010**, *110*, 447–459.
- (36) Gatel, C.; Lubk, A.; Pozzi, G.; Snoeck, E.; Hÿtch, M. Counting elementary charges on nanoparticles by electron holography. *Phys. Rev. Lett.* **2013**, *111*, 025501.
- (37) Xia, J.; Chen, F.; Li, J.; Tao, N. Measurement of the quantum capacitance of graphene. *Nat. Nanotechnol.* **2009**, *4*, 505–509.
- (38) Tsipas, P.; Giamini, S. A.; Marquez-Velasco, J.; Kelaidis, N.; Tsoutsou, D.; Aretouli, K. E.; Xenogiannopoulou, E.; Evangelou, E. K.; Dimoulas, A. Negative Quantum Capacitance Effects in Metal–Insulator–Semiconductor Devices with Composite Graphene-Encapsulated Gates. *Adv. Electron. Mater.* **2016**, *2*, 1500297.
- (39) Reiter, R.; Derra, U.; Birner, S.; Terrés, B.; Libisch, F.; Burgdörfer, J.; Stampfer, C. Negative quantum capacitance in graphene nanoribbons with lateral gates. *Phys. Rev. B: Condens. Matter Mater. Phys.* **2014**, *89*, 115406.
- (40) Fowler, R. H.; Nordheim, L. Electron Emission in Intense Electric Fields. *Proc. R. Soc. London, Ser. A* **1928**, *119*, 173–181.
- (41) de Knoop, L.; Houdellier, F.; Gatel, C.; Masseboeuf, A.; Monthieux, M.; Hÿtch, M. Determining the work function of a carbon-cone cold-field emitter by in situ electron holography. *Micron* **2014**, *63*, 2–8.
- (42) Bonard, J.-M.; Dean, K. A.; Coll, B. F.; Klink, C. Field Emission of Individual Carbon Nanotubes in the Scanning Electron Microscope. *Phys. Rev. Lett.* **2002**, *89*, 197602.
- (43) Guinea, F. Charge distribution and screening in layered graphene systems. *Phys. Rev. B: Condens. Matter Mater. Phys.* **2007**, *75*, 235433.
- (44) Kuroda, M. A.; Tersoff, J.; Martyna, G. J. Nonlinear Screening in Multilayer Graphene Systems. *Phys. Rev. Lett.* **2011**, *106*, 116804.